Optimization Design Method for Vibration Reduction of Frame Structure of Cable-Driven Parallel Robot

Da Song, Zhichao Sun, Lei Zhao, Ming Lu and Haocheng Wang
Northeast Electric Power University, Jilin, China. E-mail: songda@neepu.edu.cn

Lixun Zhang
Harbin Engineering University, Harbin, China.

(Received 16 November 2023; accepted 14 March 2024)

This paper proposes a comprehensive optimization algorithm for the crossbeam cross-section size to solve the vibration problem of the flexible cable-driven parallel robot frame. The goal is to achieve an innovative design of the cross-sectional structure. By using a differential evolution algorithm, a comprehensive scale analysis of the cross-section size of the beam is carried out. This optimization method effectively improves the cross-section moment of inertia and the bending stiffness of the beam. Additionally, based on the variable density penalty method, the topological optimization design of the cross-section is carried out under the condition of minimum flexibility, the optimization objective function is established, and the objective function is solved by the moving asymptote method. The optimization results show that the beam stiffness is maximized while meeting the minimum flexibility required by the project. Through comparative analysis with various aluminum profile structures and their constructed frames, it is verified that the cross-sectional shape obtained through the optimized design method can significantly improve the anti-vibration stability of the frame.

1. INTRODUCTION

Cable-Driven Parallel Robots (CDPRs) are a new type of parallel robot that use cables instead of rigid links. One end of each cable is connected to the end-effector, and the other end is driven by a winch, controlling the posture of the end-effector by controlling the length of the cable. Compared to ordinary parallel robots, cable-driven parallel robots have a larger workspace, a higher load-to-weight ratio, and smaller motion inertia.[1] After more than thirty years of development, they have played an important role in medical surgery,[2] rehabilitation training,[3] special operations,[4] industrial manufacturing[5] and other fields. CDPRs have attracted widespread attention due to their large workspace and high acceleration values, but CDPRs lack intuitive and generally adaptable performance evaluation indicators in the application process. Therefore, scholars like Jin and others[6] proposed a unified transmission index based on the summarization of previous work, quantitatively evaluating the motion and force transmission of CDPRs. They have verified the accuracy of the proposed indicators by carrying out motion/force analysis on fully constrained and redundant constrained CDPR. To better perform modal analysis, robustness testing, design verification and workspace estimation of cable-driven parallel robots, it is necessary to establish an accurate motion simulation model. Mamidi and Bandyopadhyay[7] had established a modular frame structure to analyze the dynamic characteristics of CDPRs and proposed a new recursive algorithm to consider the dynamic effect caused by the time-varying inertia of the cable and verified the effectiveness of the proposed frame structure using the FAST manipulator.

Additionally, in the process of building a cable-driven parallel robot, the frame structure as the main support part is indispensable. Because the end-effector of CDPRs can achieve high-speed rotation and rapid stop, when the end-effector stops suddenly, its own kinetic energy will be transmitted to the frame in a short time, causing strong vibration of the frame structure and affecting the positioning accuracy of the end-effector. Excessive vibration may seriously affect the performance of the equipment.[8,9] Therefore, various vibration suppression methods have been proposed, such as active control,[10] passive control[11] and specific control methods for specific structures.[12] Structural optimization is currently widely used to enhance vibration- damping performance.[13,14] Typical structural optimization involves finding the optimal design to minimize or maximize a certain cost function under specific constraints. Researchers such as Joubert et al.[15] carried out optimal design of uniform slender cantilever beams and plates that satisfy the Euler-Bernoulli and Kirchhoff-Love assumptions respectively. They applied the boundary variation method for the coupled optimization of the thickness and geometric shape of the plate, significantly improving the damping of linear viscoelastic structures under free vibration by means of optimal design. Scholars like Yuan et al.[16] proposed two new methods to treat the welding nodes as equivalent stiffness in response to the issue of considering many solid units at the welding joints when obtaining accurate modal parameters of conical truss sandwich beams. This method can accurately determine the modal parameters of the welding nodes and obtain their operating modal analysis results while avoiding missing modes. Guo et al.[17] analyzed the existing conical truss

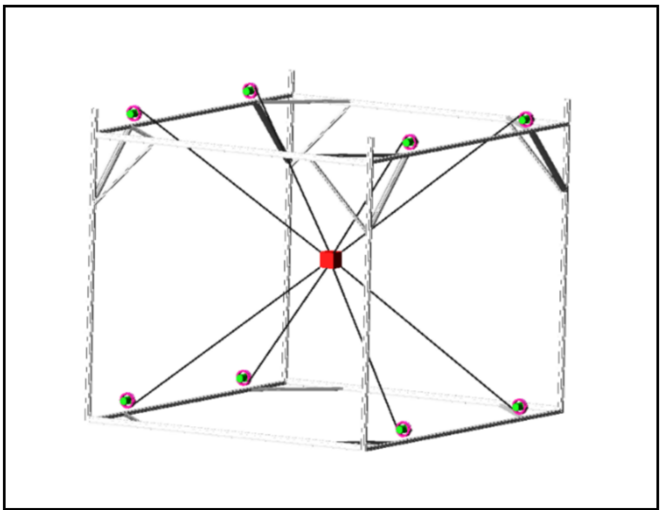

Figure 1. Cable-drive parallel robot model.

sandwich beams and proposed a new type of phononic crystal sandwich beam with an hourglass lattice structure as the core. Compared with traditional sandwich beams, the new sandwich beam can generate two additional band gaps, achieving better broadband vibration suppression. The study found that geometric parameters have a significant impact on the structural stiffness of the new sandwich beam, but have limited impact on structural quality. Therefore, the band gap of the phononic sandwich beam can be customized by adjusting structural parameters. Wu et al.[18] studied the modal coupling problem between bending, stretching and torsional deformation of cantilever beams, and established an analytical model of a rotating cantilever beam with a pretwist angle and arbitrary cross-section. The motion equation of the beam was derived using Hamilton's principle, and solved by the Rayleigh-Ritz method. The natural frequencies obtained from the analytical modal fit well with the modal natural frequencies obtained from the finite element method, proving the accuracy of the analytical model.

Among the research on the flexible cable-driven parallel robot, there is more research on workspace analysis, trajectory tracking control and vibration suppression of the end-effector, etc., while there is less research on the frame vibration of the flexible cable-driven parallel robot. Additionally, in the current frame construction process, to reduce the influence of the frame vibration problem, the installation position of the auxiliary support beam mainly relies on past experience, but lacks theoretical guidance and verification. Therefore, this paper combines the vibration reduction optimization theory of truss structure in the field of architectural engineering, starting with the construction of the beam structure of the frame, analyzes the maximum vibration amplitude of the beam structure under the action of external forces, and optimizes the cross-section shape of the beam structure, reducing the vibration response of the frame from the foundation components.

This article aims at the vibration problem generated by the frame when the cable-driven parallel robot is working and optimizes the cross-section design of the cross- beam in the frame. First, the size optimization design is carried out according to the cross-sectional shape of the crossbeam, and the cross-sectional moment of inertia of the crossbeam is taken as

Table 1. Model parameters of cable driven parallel robot framework.

Parameter	Numerical value	Parameter	Numerical value
Frame length	4 m	Pulley width	50 mm
Frame width	4 m	Pulley radius	20 mm
Frame height	4 m	Pulley depth	10 mm
Cross-section area of beam	$0.08\ \text{m} \times 0.08\ \text{m}$	Pulley angle	20°
Friction coefficient	0.6	Friction speed	100

the optimization target to improve the bending stiffness of the crossbeam. Secondly, the cross-sectional shape of the crossbeam is designed for topology optimization, and the flexibility of the crossbeam is taken as the optimization target. When the minimum flexibility required by the project is met, the overall stiffness of the crossbeam is maximized to reduce the vibration response amplitude of the crossbeam. In the second section, the vibration of the cable-driven parallel robot is analyzed. In the third section, the cross-sectional moment of inertia of the beam and the flexibility of the beam are optimized and designed respectively. Section 4 conducts comparative analysis of related examples to verify that the optimized beam has better anti-vibration stability. Finally, the article is summarized.

2. VIBRATION ANALYSIS OF CABLE-DRIVEN PARALLEL ROBOT

To optimize the design of a cable-driven parallel robot, it is necessary to establish the mechanical structure and forward and inverse dynamics models for the cable-driven parallel robot. The above model accurately reflects the tension of each cable and the vibration of each beam and frame when the end effector runs under a given trajectory.

2.1. Building the Cable-Driven Parallel Robot Model

Considering the diversity of structural types in different applications of cable-driven parallel robots,[19–21] a frame structure model with more common applications was selected in this paper.[22] This model introduced multiple auxiliary support structures based on the traditional frame, aiming to enhance the stability of the frame. Unlike the traditional frame model, this model considered the influence of several parameters of the pulley and the contact parameters between the pulley and the cables on the cable tension, thus describing the behavior of the system more accurately. These improvements will help improve the performance and reliability of the Cable-driven Parallel Robots. The specific model image is shown in Fig. 1.

Considering that the working space of the cable-driven parallel robot is related to the size of the external frame, and the increase in the size of the external frame is conducive to the control of the cable tension, making the cable transmit the driving force more smoothly, so the various parameters of the pulley were considered. In the case of the influence of the contact parameters between the cable and the cable on the tension of the cable, the parameters of the cable-driven parallel robot model are shown in Table 1.

$$\mathbf{R} = \mathbf{R}_x(\alpha)\mathbf{R}_y(\beta)\mathbf{R}_z(\gamma) = \begin{bmatrix} \cos\beta\cos\gamma & \sin\alpha\sin\beta\cos\gamma - \cos\alpha\sin\gamma & \cos\alpha\sin\beta\cos\gamma + \sin\alpha\sin\gamma \\ \cos\beta\sin\gamma & \sin\alpha\sin\beta\sin\gamma - \cos\alpha\cos\gamma & \cos\alpha\sin\beta\cos\gamma - \sin\alpha\sin\gamma \\ -\sin\beta & \sin\alpha\cos\gamma & \cos\alpha\cos\beta \end{bmatrix}. \tag{2}$$

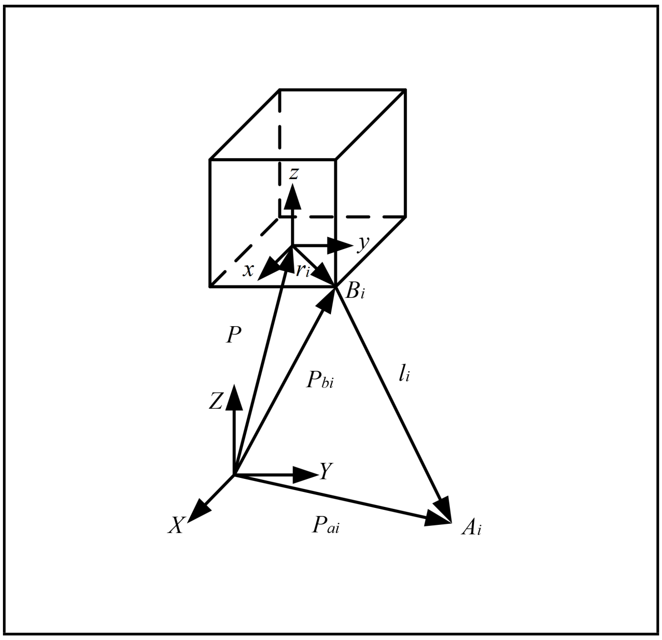

Figure 2. Simplified diagram of cable-driven parallel robot.

2.2. Optimal Distribution of Cable Tension

Based on the cable-driven parallel robot model shown in Fig. 1, a simplified diagram of the cable-driven parallel robot was established, as shown in Fig. 2. $\mathbf{A}_i$ was the connection point between the cable and the external frame, and $\mathbf{B}_i$ was the connection point between the cable and the end-effector. A global coordinate system $O-XYZ$ was established within the external frame, and a local coordinate system $o-xyz$ was established at the center position of the end-effector, with the two coordinate systems being parallel to each other. $\mathbf{l}_i$ represented the cable length, $\mathbf{P}_{ai}$ was the position vector of point $\mathbf{A}_i$ in the global coordinate system, $\mathbf{r}_i$ was the position vector of point $\mathbf{B}_i$ in the local coordinate system, $\mathbf{P}_{bi}$ was the position vector of $\mathbf{B}_i$ in the global coordinate system, and $\mathbf{P}$ was the position vector of the local coordinate system in the global coordinate system. The pose vector of the center point of the end-effector relative to the global coordinate system is: $\mathbf{q} = [x\ y\ z\ \theta_x\ \theta_y\ \theta_z]^T$.

According to the closed vector quadrilateral method, the lengths of each cable can be obtained as follows:

$$\mathbf{l}_i = \mathbf{P}_{ai} - \mathbf{P} - \mathbf{R}\mathbf{r}_i; \tag{1}$$

where $\mathbf{R}$ was the rotation matrix, given by Eq. (2).

The static equilibrium equation of the cable-driven parallel robot can be obtained as follows:

$$\begin{cases} \sum_{i=1}^{N} \mathbf{f}_i = -\mathbf{F}; \\ \sum_{i=1}^{N} \mathbf{r}_i \times \mathbf{f}_i = -\mathbf{M}; \end{cases} \tag{3}$$

where $\mathbf{f}_i$ and $\mathbf{r}_i \times \mathbf{f}_i$ were the cable tension and the torque generated by the cable tension, respectively, and $\mathbf{F}$ and $\mathbf{M}$ were the external force and torque experienced by the end-effector, respectively. The equation was rewritten in matrix form as follows:

$$\mathbf{WF} = \boldsymbol{\omega}; \tag{4}$$

where $\mathbf{W}$ was the structure matrix:

$$\mathbf{W} = \begin{bmatrix} \mathbf{u}_i \\ \mathbf{r}_i \times \mathbf{u}_i \end{bmatrix}; \tag{5}$$

where $\mathbf{u}_i = |\mathbf{l}_i / l_i|$ was the unit vector of the i-th cable.

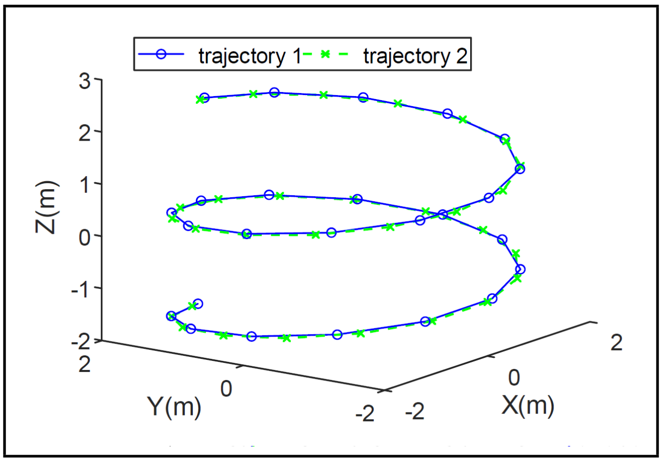

Figure 3. End effector motion trajectory diagram.

In the preliminarily determined model of the CDPRs, the rotational torque of the pulley was taken as the input variable, and the displacement in all directions of the end-effector was taken as the output variable. Given the motion trajectory of the end-effector, the maximum tension of each cable under different trajectories was obtained through Newton's iterative method.[23,24] The motion trajectory of the end-effector was given as:

$$\begin{cases} X_1 = 2 * \sin(2\pi t_1); \\ Y_1 = 2 * \cos(2\pi t_1); \\ Z_1 = 2 - 0.625 * t_1; \end{cases} \quad \begin{cases} X_2 = 2 * \sin(2\pi t_2); \\ Y_2 = 2 * \cos(2\pi t_2); \\ Z_2 = 2 - 0.625 * (t_2 - 6.25). \end{cases} \tag{6}$$

This trajectory was divided into two parts, from 0 to 6.25 seconds, the end-effector spirals downward, and from 6.25 to 12.5 seconds, the end-effector spirals upward. The motion graph is shown in Fig. 3.

Under the given trajectory, the tension graph of each cable of the CDPRs obtained through simulation is shown in Fig. 4.

According to the tension graph of the cable shown in Fig. 4, when the end-effector runs along the given track, the maximum tension of the cable does not exceed 1800 N. Therefore, in the beam vibration analysis in Section 3, the external excitation received by the beam vibration can be taken as 1800 N.

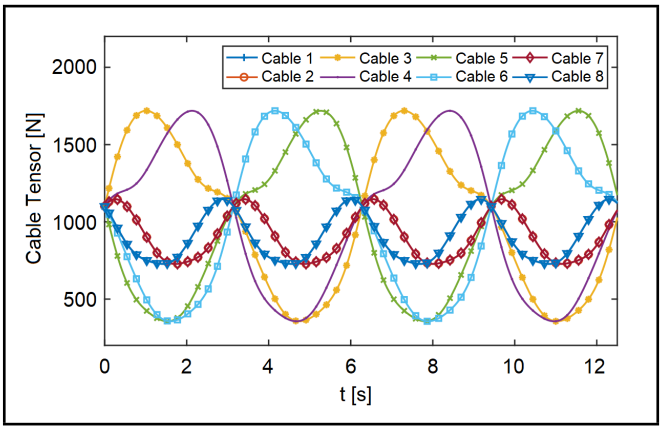

Figure 4. Cable tension image.

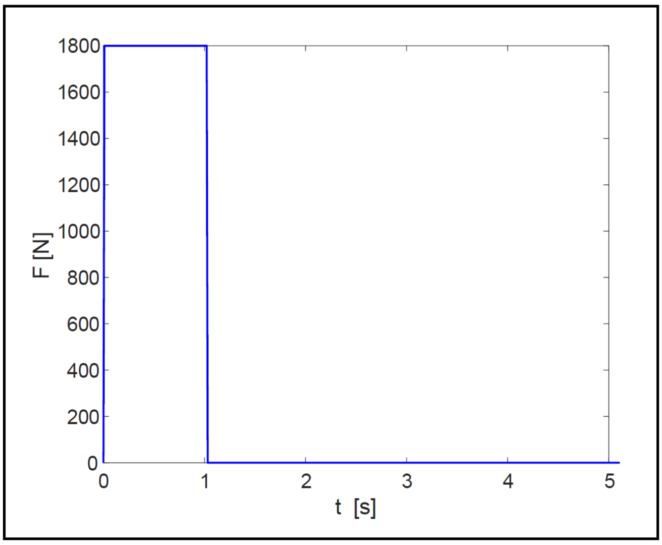

Figure 5. External force images.

2.3. Vibration Analysis of CDPR

2.3.1. Beam Vibration Analysis

During the movement of the CDPR, the sudden start and stop of the end-effector will cause a sharp change in the tension of the cable. The sharp change in tension will cause strong vibration of the frame. According to the maximum tension of the cable determined in Fig. 4, combined with the feature of short tension change time, the external excitation can be simplified to a step function of 1800 N lasting for 1 second. The external force image is shown in Fig. 5 .

In the process of building the frame of the CDPR, the four types of cross-sectional shapes of aluminum profiles shown in Fig. 6 are commonly used.

Finite element analysis of beams with four different cross-sectional shapes was carried out to observe the overall vibration response of beams with different cross-sections under load. During the construction process of the frame of the CDPR, the beams were fixedly connected through angle irons and bolts, so when performing finite element analysis, the beam was considered as a fixed beam, and fixed constraints were added to both ends of the beam. Relevant parameters such as elastic modulus, density, and Poisson's ratio were filled in according to the properties of the aluminum profile, as shown in Table 2.

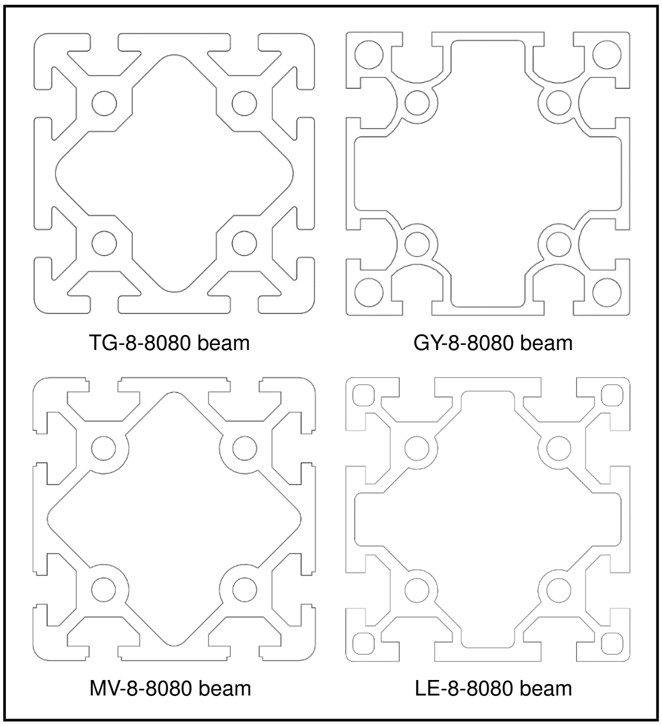

Figure 6. Cable driven parallel robot beam image.

Table 2. Aluminum profile material properties.

Attribute	Numerical value	Unit
Density	2.69	kg·m^{-3}
Elastic modulus	6.9×10^{10}	Pa
Poisson's ratio	0.3	

Table 3. Maximum vibration deformation of beam.

Beam type	Maximum deformation value [m]
TG-8-8080 beam	0.0083046
GY-8-8080 beam	0.010648
MV-8-8080 beam	0.0082421
LE-8-8080 beam	0.0094645

According to the model shown in Fig. 1, the installation position of the pulley on the beam was the application point of the tension of the cables, the size of the force was as shown in Fig. 5, the direction of the force was along the direction of the cables, and the vibration response diagram of the beam was obtained after finite element analysis, as shown in Fig. 7.

As can be seen from Fig. 7, the maximum vibration amplitude of each aluminum profile mainly occurred at the center position, and Table 3 summarizes the maximum vibration amplitude of each aluminum profile.

2.3.2. Frame Vibration Analysis

In the previous section, vibration analysis was conducted on four different cross-sectional shapes of aluminum profiles. In this section, vibration analysis will be conducted on frames constructed using four different cross-sectional shapes of aluminum profiles. When conducting vibration analysis on the frame structure, due to the limitations of hardware facilities, the structure of the frame structure has been relatively simplified. The simplified frame vibration analysis image is shown in Fig. 8.

Combined with the data analysis results in Table 3 and Table 4, the vibration of the aluminum beam and frame con-

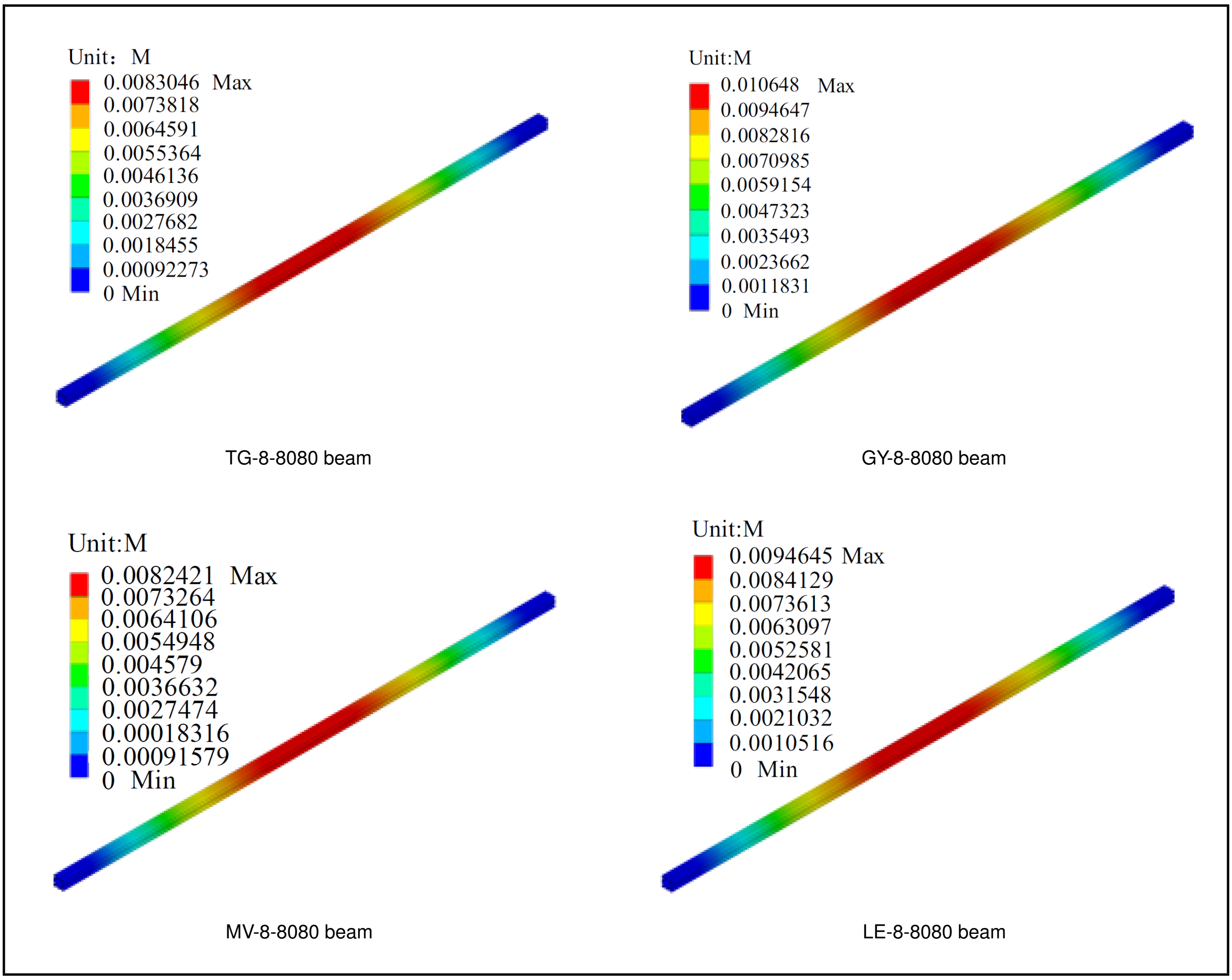

Figure 7. Vibration deformation image of beam.

Table 4. Maximum vibration deformation of frame.

Frame type	Maximum deformation value [m]
TG-8-8080 frame	0.077597
GY-8-8080 frame	0.07592
MV-8-8080 frame	0.090387
LE-8-8080 frame	0.086607

structed by the aluminum profiles is comprehensively analyzed. It can be concluded that among the four kinds of aluminum profiles, the vibration response amplitude of the LE-8-8080 aluminum profile is the smallest. This paper will optimize the design of the LE-8-8080 aluminum profile to further improve the stiffness of aluminum profile and reduce its vibration response amplitude.

3. OPTIMIZATION OF CROSSBEAM STRUCTURE

3.1. Cross-Sectional Structural Analysis of Aluminum Profiles

Aluminum profiles are mainly affected by the bending moment and torque in the process of use, it is necessary to ensure its performance, that is, the bending and torsional resistance of aluminum profiles, in the case of aluminum profile model selection, the bending and torsional resistance of the following formula can be known that its bending and torsional performance depends on the section moment of inertia:

$$\tau_{\max} = \frac{T\rho_{\max}}{I_p} = \frac{T}{W_t}; \tag{7}$$

$$\sigma_{\max} = \frac{My_{\max}}{I_z} = \frac{M}{W_z}; \tag{8}$$

where: W_t, W_z are the bending and torsional section coefficients respectively, which are quantities related only to the section size. Therefore, the moment of inertia of the cross-section of the selected aluminum alloy profile is used as an indicator to improve its bending performance. Figure 9(a) shows the cross-sectional shape of the aluminum profile that will be optimized, determined in Section 2, and the specific dimensions have been marked.

Since the structure shown in Fig. 9(a) is a centrally symmetrical figure, only 1/4 of the cross-section needs to be analyzed. Taking the upper right corner of the cross-section as an example, the selected cross-section design variables are shown in Fig. 9(b), and the value range and initial values of the design variables limited by the cross-section wall thickness requirements are shown in Table 5.

In the process of structural design and calculation, it was

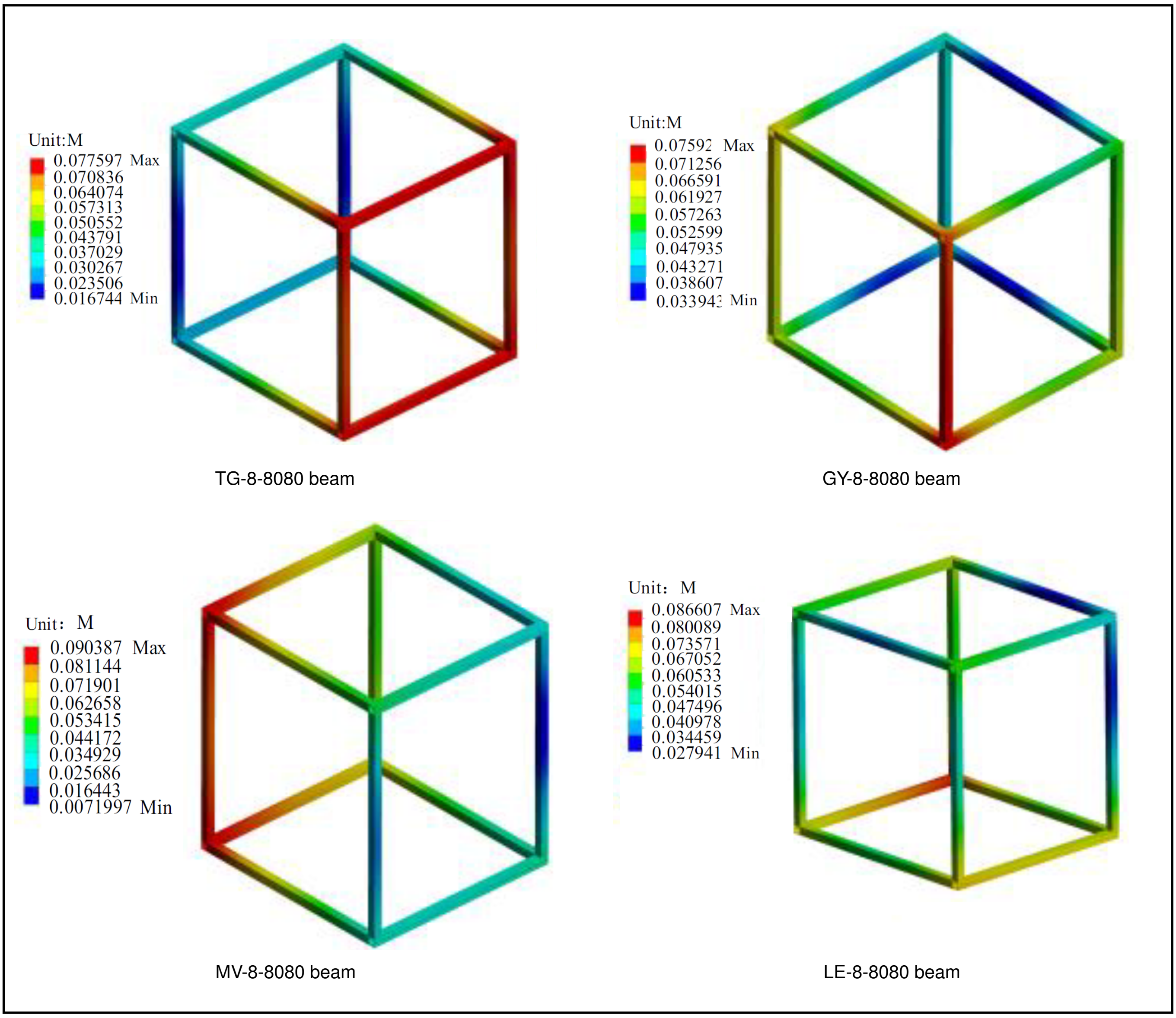

Figure 8. Frame vibration deformation image.

Table 5. Design variable value range.

Design variable	Design interval	Initial value [m]
a	[2.4 4.4]	3.4
b	[5 7]	6

necessary to calculate the bending stiffness of the cross-section of the crossbeam around the x-axis and y-axis respectively under the action of bending moment, to meet the requirements for the use of the crossbeam. The moment of inertia was the integral of the area of each element of the cross-section and the quadratic product of the distance of each microelement to a specified axis on the cross-section, which can be expressed as:

$$I_x = \int y^2 dA; \tag{9}$$

$$I_y = \int x^2 dA; \tag{10}$$

According to Eqs. (9) and (10), the moment of inertia of the cross-section of the figure shown in Fig. 10 can be obtained as:

$$I_x = -\frac{\pi a^4}{16} - 4900\pi a^2 - \frac{b^4}{3} - 1600b^2 + 2275554.6; \tag{11}$$

$$I_y = -\frac{\pi a^4}{16} - 4900\pi a^2 - \frac{b^4}{3} - 1600b^2 + 2275554.6; \tag{12}$$

According to Eqs. (11) and (12), the cross-sectional moment of inertia about the x-axis was equal to the cross-sectional moment of inertia about the y-axis due to the symmetry of the center of the structure.

3.2. Optimization Method of Aluminum Profile Cross-Section Moment of Inertia

The design objective of the optimization problem in this paper is to maximize the moment of inertia I of the aluminum profile cross-section, and the constraint is the range of design variable values. According to Table 6, the optimization parameters of the beam are a and b, and the vector relationship of the optimization parameters is:

$$x = [a \;\; b]. \tag{13}$$

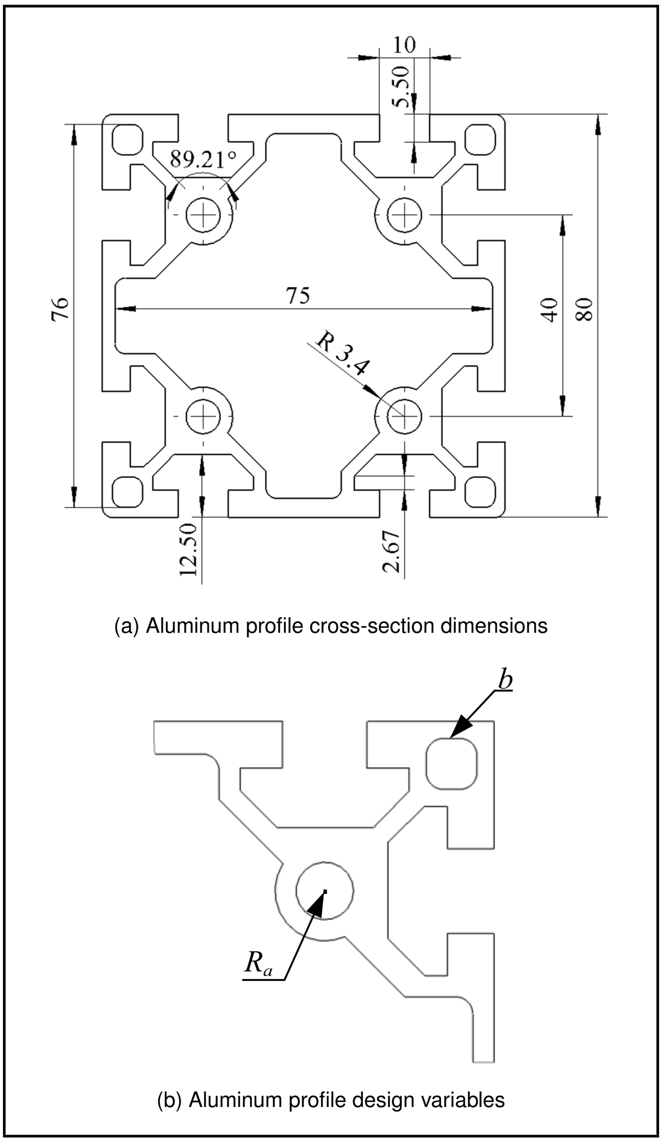

Figure 9. Aluminum profile cross-section shape.

According to Eqs. (11) and (12), the moment of inertia of the cross-section of the beam about the x-axis is equal to that about the y-axis, so the moment of inertia of the cross-section about the x-axis was taken as the objective function to find the maximum value of the moment of inertia of the aluminum profile cross-section. The expression of the objective function is:

$$\text{max: } f(x) = -\frac{\pi a^4}{16} - 4900\pi a^2 - \frac{b^4}{3} - 1600b^2 + 2275554.6. \tag{14}$$

Considering the size of the wall thickness of the aluminum profile, the change of the design variables needed to be within the range of the wall thickness. Therefore, this condition was met by constraining the range of the design variable values. So, the constraint conditions are as follows:

$$\begin{cases} 2.4 \le a \le 4.4; \\ 5 \le b \le 7. \end{cases} \tag{15}$$

So, the overall topological optimization mathematical model is:

$$\begin{aligned} &\text{Find } x = [x_1, x_2, \ldots, x_n]^T \\ &\max f(x) = -\frac{\pi a^4}{16} - 4900\pi a^2 - \frac{b^4}{3} - 1600b^2 + 2275554.6 \\ &\text{s.t. } \begin{array}{c} 2.4 \le a \le 4.4; \\ 5 \le b \le 7. \end{array} \end{aligned} \tag{16}$$

To solve the above topological optimization mathematical model, this paper used the differential evolution algorithm.[25–28] The differential evolution method is essentially a real-number genetic algorithm, which has all the characteristics of a genetic algorithm, but has been significantly modified based on the original real-number genetic algorithm, giving it strong global convergence ability and robustness. The process of using the differential evolution algorithm to solve the objective function is as follows:

1) Setting control parameters
Set the population size to Np, the mutation factor to F, the crossover factor to C_r, the dimension to D, and randomly generate the initial population $X(0) = [x_1^{(0)}, x_2^{(0)}, \ldots, x_{Np}^{(0)}]$.

2) Mutation
For each target vector $x_{i,G}$ $(i = 1, 2, \ldots, Np)$, the basic differential scheme algorithm generates the mutation vector according to the following formula:

$$v_{i,G} = x_{r_1,G} + F \cdot (x_{r_2,G} - x_{r_3,G}). \tag{17}$$

In the equation above: the randomly selected indices r_1, r_2, and r_3 must be distinct, and must also differ from the target vector index i. Thus, it was necessary to satisfy $Np > 4$. The mutation operator F was a real constant factor, ranging within $[0, 2]$, which controls the scaling of the deviation variable.

3) Crossover
The mutated individual was probabilistically selected in a certain way with another individual from the current population:

$$U_i^G = \begin{cases} U_{j,i}^G & \text{rand}(j,i) \le C_r; \\ X_{j,i}^G & \text{rand}(j,i) > C_r. \end{cases} \tag{18}$$

Here, $\text{rand}(j,i)$ $(i \in [1, Np]$, $j \in [1, D])$ was a random number uniformly distributed in the interval $[0, 1]$. C_r is the crossover factor, and $C_r \in [0, 1]$.

4) Selection
The individual produced by "crossover" was compared with the individuals from the initial population. The better ones are retained:

$$X_i^{G+1} = \begin{cases} U_{j,i}^G & f(U_i^G) \le f(X_i^G); \\ X_{j,i}^G & f(U_i^G) > f(X_i^G); \end{cases} \tag{19}$$

where: $f(x)$ represented the objective function value of the population individual; $i = 1, 2, \ldots, Np$.

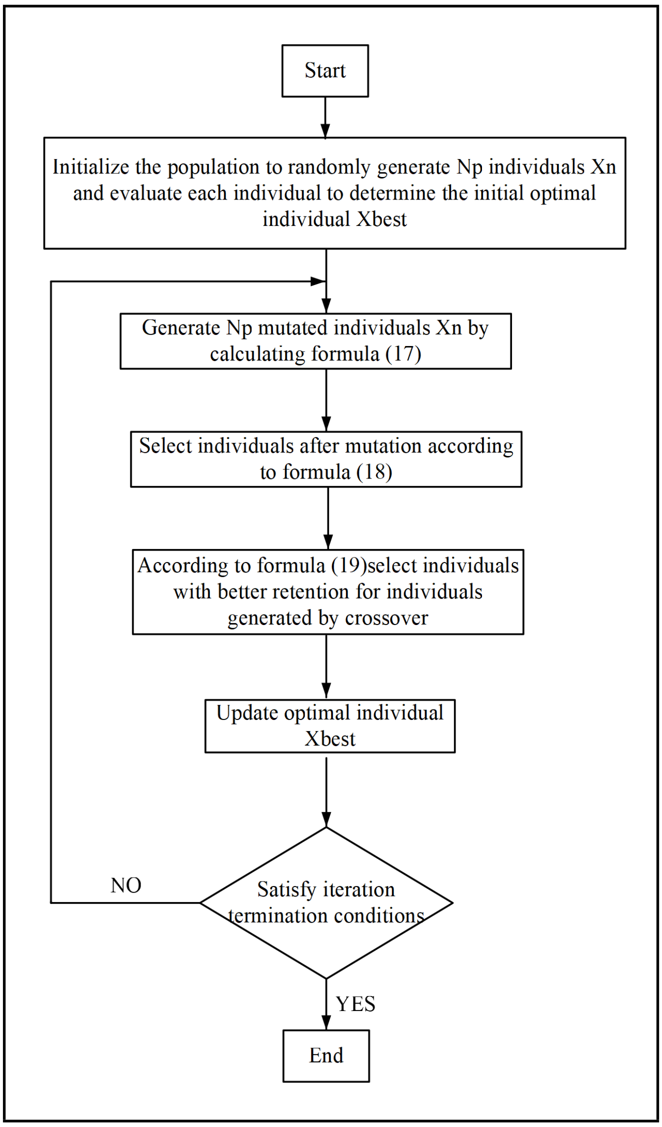

Figure 10. Differential evolution algorithm flowchart.

Table 6. Design variable optimal solution.

Design variables	Optimal solution [mm]
a	2.4
b	5

The optimization process diagram is shown in Fig. 10.

The differential evolution algorithm was used to optimize the objective function, thus solving for the design variables. The optimization parameters were set as: population size $Np = 20$, mutation factor $F = 0.5$, crossover factor $C_r = 0.1$, and maximum evolution generation $G = 100$. The optimal solution of the design variables obtained by inputting the design variables and section parameter model into the optimization algorithm is shown in Table 6.

The graphs of the objective function and the iterative process are shown in Fig. 11 and Fig. 12.

After obtaining the optimal solution that meets the requirements through the differential evolution algorithm, it was substituted into Eqs. (11) and (12) to obtain the optimized section moment of inertia.

As can be seen from Table 7, by comparing the results before and after, it is found that the moment of inertia of the optimized cross-section has increased by 5% compared with that before optimization. The bending stiffness of the crossbeam has been further improved.

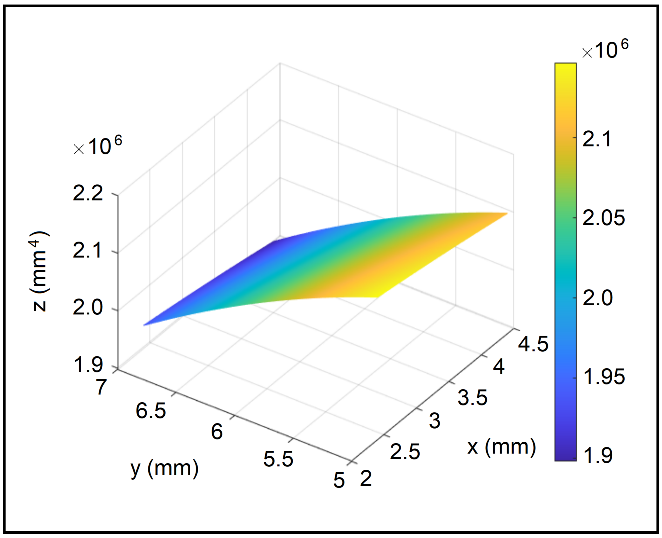

Figure 11. Objective function image.

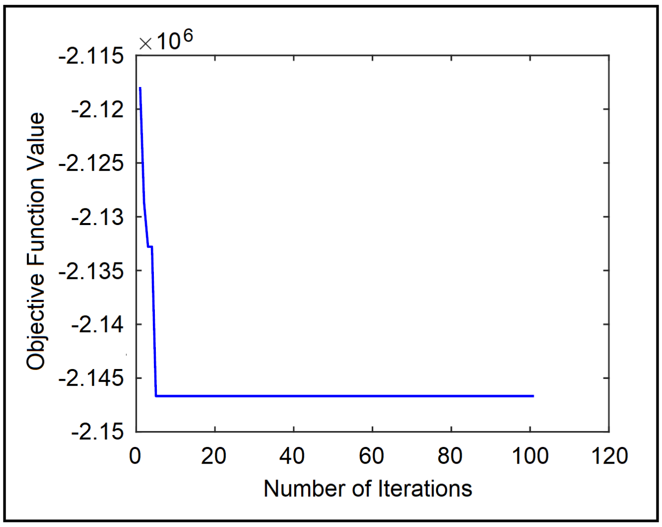

Figure 12. Iterative image.

Table 7. Optimal results.

	I_x [mm^4]	I_y [mm^4]
Before optimization	2103350	2013350
After optimization	2146670	20146670

3.3. Optimization Method for Aluminum Profile Compliance

Based on the optimized beam obtained in Section 2, the overall stiffness was optimized, and the flexibility of the beam was selected as the optimization target. The volume of the material was selected as the constraint condition, and the maximum stiffness was achieved when the minimum flexibility required for engineering needs was reached. The SIMP model[29–32] was adopted, and the artificial density ρ_i was introduced as the design variable:

$$X = [\rho_1, \rho_2, \ldots, \rho_i, \ldots, \rho_n]. \tag{20}$$

The relationship between the discrete unit and the elastic modulus was established using the unit pseudo-density, and the formula for the variable density material interpolation model is:

$$E_i(\rho_i) = E_{\min} + \rho_i^p (E_0 - E_{\min}); \tag{21}$$

where: $E_i(\rho_i)$ represented the actual elastic modulus of the i-th unit, p was a penalty parameter, generally taken as $3 \sim 6$. E_0 was the elastic modulus of the solid material, set to 1. $E_{\min}$ was the elastic modulus of the blank material, generally a small number close to zero. Based on the SIMP model, the change of the elastic modulus $E_i(\rho_i)$ can be driven by the iterative update of ρ_i, and then finite element analysis was carried out.

Therefore, the total stiffness matrix and structural objective function of the SIMP model can be expressed as:

$$K(x) = \sum_{i=1}^{N} [E_{\min} + \rho_i^p \Delta E] K(p_i); \tag{22}$$

$$C(x) = \sum_{i=1}^{N} [E_{\min} + \rho_i^p \Delta E][U_i]^T [K_i][U_i]; \tag{23}$$

where U and F were the total displacement direction vector and the direction vector of the external force related to the structure respectively, and K was the total stiffness matrix.

3.4. Method of Moving Asymptotes Based on SIMP Model

The Solid Isotropic Material with Penalization (SIMP) method was used to establish a minimum compliance objective function. The method of moving asymptotes (MMA)[33–36] is applied to solve the topology optimization problem. The mathematical expression is as follows:

$$\begin{aligned}
&\text{Find:} && \rho_i = [\rho_1, \rho_2, \ldots, \rho_n]^T \in R^n, y_1 \in R^n, z \in R \\
&\text{min:} && \sum_{i=1}^{N} \rho_i^p u_i^T k_0 u_i + z + 1000 y_1 \\
&\text{s.t.:} && \sum_{i=1}^{N} \rho_i - fV - y_1 \le 0; \\
& && 0 < \rho_{\min} \le \rho_i \le 1 \quad (i = 1, 2, \ldots, n); \\
& && y_i \ge 0; \quad z \ge 0;
\end{aligned} \tag{24}$$

where ρ_i represented the design variables of the material, which was the relative density of the material. n was the number of finite elements within the design domain. y, z were the additional design variables. k_0 was the stiffness matrix when the element density $\rho_i = 1$. u_i was the displacement vector of the i-th element. f was the given ratio of relative volumes between different materials. V_0 was the relative volume of the initial material structure. $\rho_{\min}$ was the minimum relative density (in this article, $\rho_{\min} = 0.01$). The calculation process of topology optimization of continuum structure based on MMA algorithm is as follows:

1) Construct the structural topology optimization problem into the solution form of the MMA standard algorithm.

2) Select initial iteration values of design variables.

3) Calculate the function values and sensitivity values of the objective function and constraint function corresponding to the independent variables.

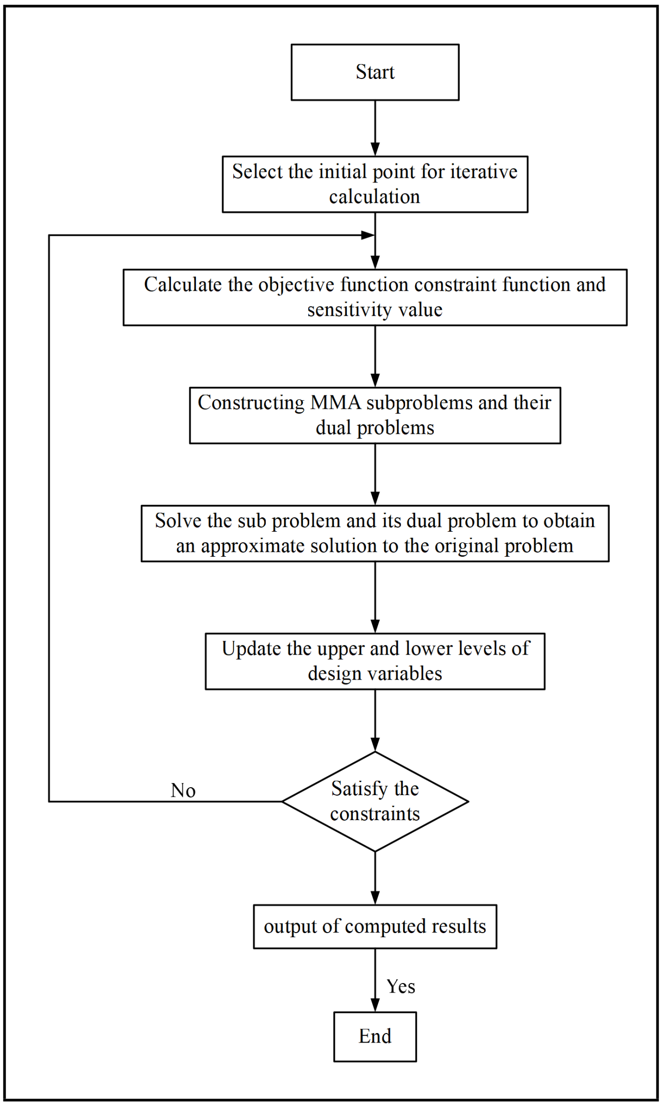

Figure 13. Method of moving asymptotes flowchart.

4) Construct the MMA sub-problem and its dual problem, and solve them to obtain an approximate solution to the original problem.

5) Update the upper and lower moving limits of the design variables.

6) Determine whether the result meets the given convergence conditions. If not, return to step (3) for a new cycle. If it matches, end the loop and output the result.

The algorithm flow chart designed in this paper is as Fig. 13.

This paper focuses on optimizing the cross-sectional shape of the beam to improve the overall stiffness of the beam. The cross-sectional size of the beam was (0.08 m × 0.08 m), grid division density was 80 × 80. The endpoints of the cross-section were fixed, and an external force of 1800 N was applied at the center of the cross-section. The Young's modulus E of the beam was 2.1×10^5, and the Poisson's ratio σ was 0.3. The objective function is to minimize the total compliance of the structure, with the constraint that the volume fraction does not exceed 50%. The penalty factor p was 3, and the filter radius $r_{\min}$ was 1.2.

Using the MMA based on the SIMP method, after 53 iterations (The computer configuration used in this paper was

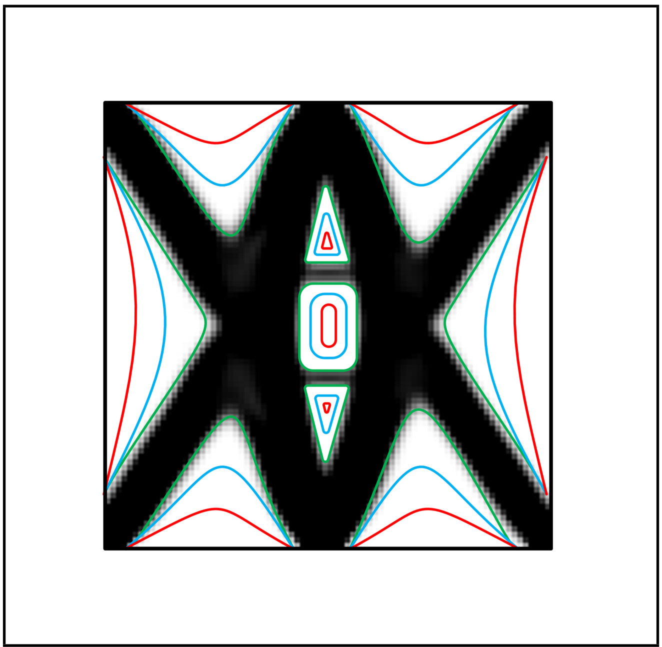

Figure 14. Topology optimization results.

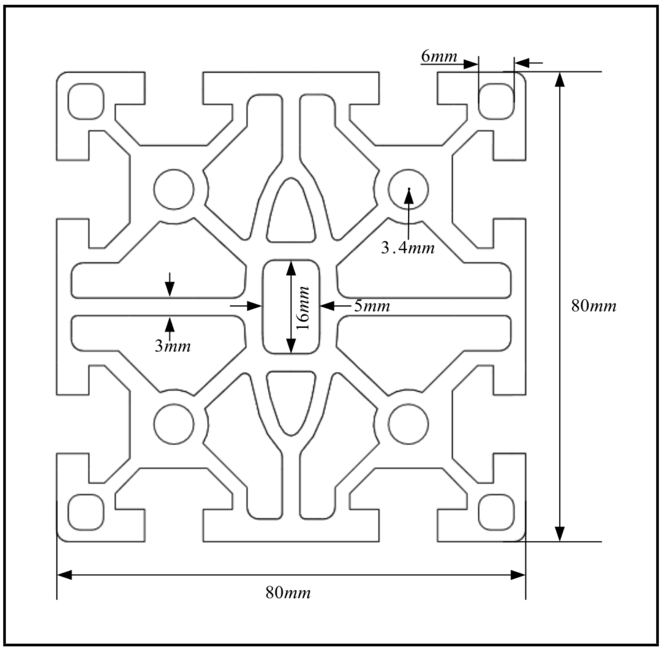

Figure 16. Schematic diagram of optimized crossbeam.

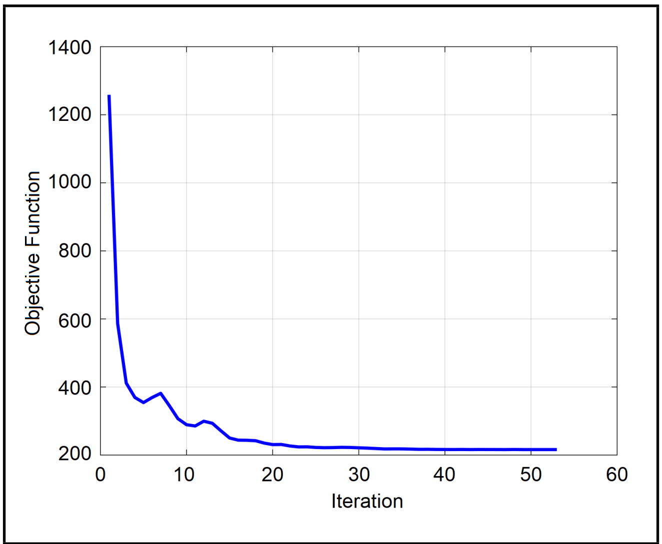

Figure 15. Iterative image.

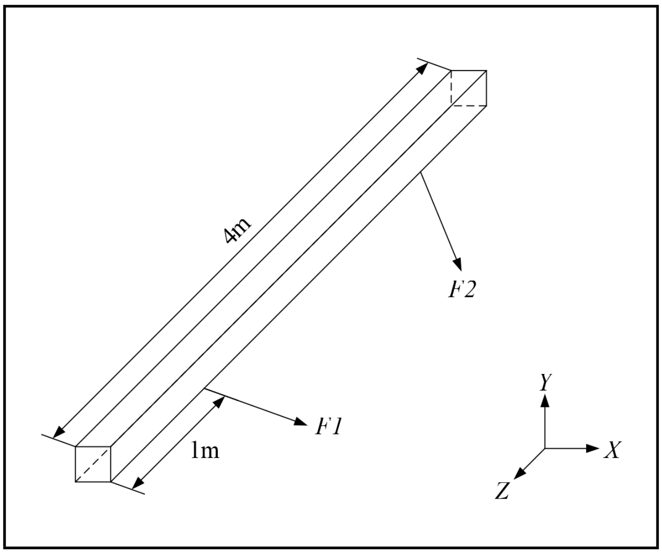

Figure 17. Cross beam force diagram.

Intel®Core™ i5-11400H, with 16.0 GB memory), an average compliance of 216.347 was obtained. The optimized structure diagram and optimization iteration process are shown in Fig. 14 and Fig. 15 respectively.

After modeling the optimized beam structure, the schematic diagram of the beam structure as shown in Fig. 16 is obtained.

4. NUMERICAL ANALYSIS

The cross-sectional moment of inertia and the overall compliance of the LE-8-8080 aluminum profile were optimized and analyzed, and the cross-sectional shape as shown in Fig. 16 was obtained. According to the data of the cross-sectional drawing, the sketch is first drawn, the solid model of the optimized beam is established, and the vibration simulation analysis is carried out. According to the cable-drive parallel robot model shown in Fig. 1, the optimization beam adds fixed constraints to its two ends during the analysis process, the installation position of the pulley is used as the action point of the cable on the beam, the tension of the cable is shown in Fig. 5, and the direction of the force is along the direction of the cable. The force diagram of the beam is shown in Fig. 17.

In the simulation analysis of the optimized beam and various types of beams, the vibration amplitude of each point is observed every 0.2 m in the direction of the length of the beam, and the specific beam separation image is shown in Fig. 18.

Through the vibration simulation analysis of each beam, the vibration response image of each point in the beam is obtained as shown in Fig. 19.

The vibration response of the beam in the x and y directions (transverse to the beam) shown in Fig. 19 is relatively obvious, while the order of magnitude of the vibration response along the Z direction (axial to the beam) is less than 10^{-5}, so it is ignored here. The image in Fig. 19 shows that the vibration response amplitude at the middle position of various crossbeams is the highest and gradually decreases towards

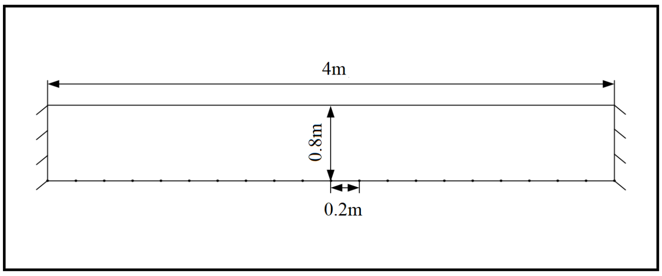

Figure 18. Separation image of each point on the crossbeam.

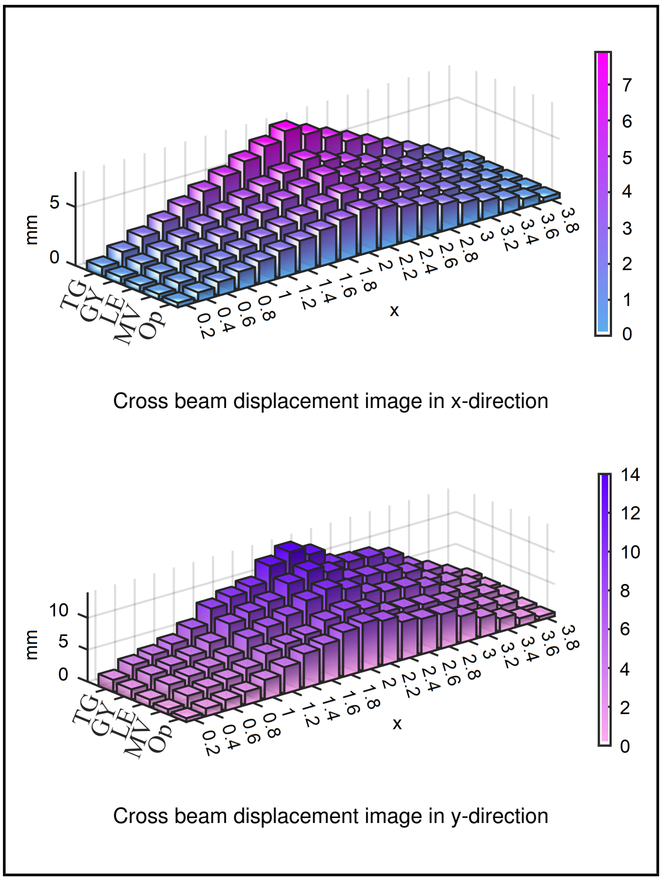

Figure 19. Vibration deformation images of beams in various directions.

both ends. Compared to traditional beam structures, the optimized beam has the smallest vibration response amplitudes at each point in the x and y directions. From this, it can be concluded that the optimized crossbeam structure has high stability in terms of vibration resistance.

The optimized crossbeam was used to construct a cable-driven parallel robot frame structure for vibration analysis. To ensure the rigor of the comparison with the traditional frame, in addition to replacing the main beam, other factors such as the number of auxiliary supports, the configuration of the frame, and the stress point and force size of the frame have not changed. The simulation analysis of the built frame is carried out, and the simulation results as shown in Fig. 20 are obtained.

The relationship between modal order and vibration deformation is critical to understanding and optimizing the performance of the beam. Therefore, in Fig. 20, the modal analysis of various types of beams is carried out, and their vibration deformation in different modes is studied in detail. It can be observed from the figure that in the first seven modes, no matter what type of beam, their vibration deformation increases according to the law of increasing order. However, this trend changes as soon as the modal order exceeds the seventh order, and the vibration deformation begins to decline step by step. This phenomenon shows that the modal order plays a significant role in the vibration deformation process of the beam. In this case, the cable-driven parallel robot frame constructed using optimized crossbeams has the smallest vibration deformation at each mode. The results show that the frame structure with optimized beams can significantly improve the anti-vibration stability of the frame.

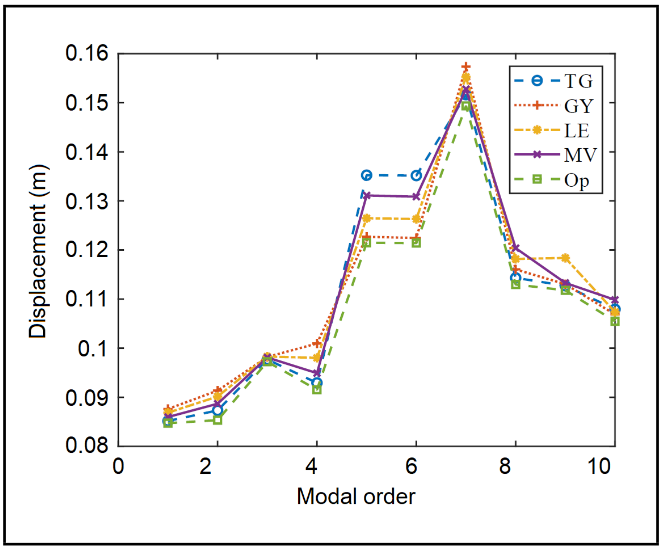

Figure 20. Modal deformation images of each order of the frame.

5. CONCLUSIONS

This paper focuses on the vibration problem of the cable-driven parallel robot frame structure and optimizes the crossbeam structure in the frame structure. In the design process, the differential evolution algorithm is used to optimize the cross-sectional dimensions of the crossbeam, and the parameters in the cross-section are optimized by constructing an objective function. The optimization results show that this optimization method can effectively improve the moment of inertia of the crossbeam cross-section and thus enhance the bending stiffness of the crossbeam. Additionally, this paper introduces a new overall stiffness topological optimization algorithm for the crossbeam. This algorithm aims to minimize the flexibility of the crossbeam structure and uses the Solid Isotropic Material with Penalization method to build the topological optimization model. The method of moving asymptotes is used to solve the model, thereby obtaining the ideal crossbeam cross-sectional shape. Finally, a comprehensive comparative analysis is conducted between the optimized crossbeam structure and four different types of aluminum profile crossbeams. Simulation data verifies that the optimized crossbeam structure can significantly reduce vibration response. This result is applicable not only to single crossbeams but also to the overall frame structure composed of crossbeams, confirming the excellent performance of the optimized crossbeam in vibration control. These findings provide important guidance and theoretical support for the design of cable-driven parallel robot frame structure.

ACKNOWLEDGEMENTS

The authors express their gratitude to:

1) National Natural Science Foundation of China (Grant No. 61773007).
2) Jilin Provincial Natural Science Foundation of China (Grant No. YDZJ202301ZYTS272).

REFERENCES

[1] Qian, S., Zi, B., Shang, W. W., and Xu, Q. S. A review on cable-driven parallel robots, *Chinese Journal of Mechanical Engineering*, **31** (1), 1–11, (2018). https://doi.org/10.1186/s10033-018-0267-9

[2] Nelson, C. A. A modular cable-driven surgical robot with a safe joint design, *Mechanism Design for Robotics: Proceedings of the 4th IFToMM Symposium on Mechanism Design for Robotics*, 77–84, (2019). https://doi.org/10.1007/978-3-030-00365-4_10

[3] Li, Z., Li, W., Chen, W. H., Zhang, J., Wang, J., Fang, Z., and Yang, G. Mechatronics design and testing of a cable-driven upper limb rehabilitation exoskeleton with variable stiffness, *Review of Scientific Instruments*, **92** (2), (2021). https://doi.org/10.1063/5.0037317

[4] Bu, W., Zhou, W., Fang, L., Chen, J., An, X., and Huang, J. A novel cable-driven parallel robot for inner wall cleaning of the large storage tank. *Advances in Mechanical Design: Proceedings of the 2019 International Conference on Mechanical Design (2019 ICMD)*, 28–40, (2020). https://doi.org/10.1007/978-981-32-9941-2_3

[5] Jung, J. Workspace and stiffness analysis of 3D printing cable-driven parallel robot with a retractable beam-type end-effector, *Robotics*, **9** (3), 65, (2020). https://doi.org/10.3390/robotics9030065

[6] Jin, X., Ye, W., and Li, Q. New indices for performance evaluation of cable-driven parallel robots: Motion/force transmissibility, *Mechanism and Machine Theory*, **188**, 105402, (2023). https://doi.org/10.1016/j.mechmachtheory.2023.105402

[7] Mamidi, T. K. and Bandyopadhyay, S. A computational framework for the dynamic analyses of cable-driven parallel robots with feed and retrieval of cables, *Mechanism and Machine Theory*, **186**, 105338, (2023). https://doi.org/10.1016/j.mechmachtheory.2023.105338

[8] Krivošej, J., Beneš, P., Zavřel, J., Balon, A., Halamka, V., and Šika, Z. Energy efficient robots based on structures with tensegrity features and cable-driven mechanisms, *Mechanism and Machine Theory*, **187**, 105364, (2023). https://doi.org/10.1016/j.mechmachtheory.2023.105364

[9] Chawla, I., Pathak, P. M., Notash, L., Samantaray, A. K., Li, Q., and Sharma, U. K. Inverse and forward kineto-static solution of a large-scale cable-driven parallel robot using neural networks, *Mechanism and Machine Theory*, **179**, 105107, (2023). https://doi.org/10.1016/j.mechmachtheory.2022.105107

[10] Shi, X., Guan, X., Shen, W., and Xing, L. A control strategy using negative stiffness and semi-active viscous damping for fully tracking active control force for bridge cables: Principles and simulations, *Structural Control and Health Monitoring*, **29** (9), e2989, (2022). https://doi.org/10.1002/stc.2989

[11] Hu, J., Zhuang, Y., Zhu, Y., Meng, Q., and Yu, H. Intelligent parametric adaptive hybrid active–passive training control method for rehabilitation robot, *Machines*, **10** (7), 545, (2022). https://doi.org/10.3390/machines10070545

[12] Sun, L., Yin, W., Wang, M., and Liu, J. Position control for flexible joint robot based on online gravity compensation with vibration suppression, *IEEE Transactions on Industrial Electronics*, **65** (6), 4840–4848, (2017). https://doi.org/10.1109/TIE.2017.2772157

[13] Zhao, Z., Meng, W., Yan, B., Yang, T., Ren, H., and Yuan, Y. Optimization design of vibration reduction structure of driving sprocket based on niche adaptive genetic algorithm, *International Journal of Acoustics and Vibration*, **27** (2), (2022). https://doi.org/10.20855/ijav.2022.27.21851

[14] Liu, Y., Liu, J., Pan, G., Guo, L., and Huang, Q. A design method for vibration and acoustic reduction of the power system in an underwater automobile glider, *International Journal of Acoustics and Vibration*, **27** (3), (2022). https://doi.org/10.20855/ijav.2022.27.31865

[15] Joubert, A., Allaire, G., Amstutz, S., and Diani, J. Damping optimization of viscoelastic cantilever beams and plates under free vibration, *Computers and Structures*, **268**, 106811, (2022). https://doi.org/10.1016/j.compstruc.2022.106811

[16] Yuan, K. and Zhu, W. Modeling of welded joints in a pyramidal truss sandwich panel using beam and shell finite elements, *Journal of Vibration and Acoustics*, **143** (4), 041002, (2021). https://doi.org/10.1115/1.4048792

[17] Guo, Z., Wen, J., Yu, D., Hu, G., and Yang, Y. Widening the band gaps of hourglass lattice truss core sandwich structures for broadband vibration suppression, *Journal of Vibration and Acoustics*, **145** (6), (2023). https://doi.org/10.1115/1.4063443

[18] Wu, X., Jiao, Y., and Chen, Z. An analytical model of a rotating radial cantilever beam considering the coupling between bending, stretching, and torsion, *Journal of Vibration and Acoustics*, **144** (2), 021004, (2022). https://doi.org/10.1115/1.4051494

[19] Sun, H., Tang, X., Hou, S., and Wang, X. Vibration suppression for large-scale flexible structures based on cable-driven parallel robots, *Journal of Vibration and Control*, **27** (21–22), 2536–2547, (2021). https://doi.org/10.1177/1077546320961948

[20] Zhang, Z., Shao, Z., and Wang, L. Optimization and implementation of a high-speed 3-DOFs translational cable-driven parallel robot, *Mechanism and Machine Theory*, **145**, 103693, (2020). https://doi.org/10.1016/j.mechmachtheory.2019.103693

[21] Sanjeevi, N. S. S. and Vashista, V. Stiffness modulation of a cable-driven serial-chain manipulator via cable routing alteration, *Journal of Mechanisms and Robotics*, **15** (2), 021009, (2023). https://doi.org/10.1115/1.4054612

[22] Meziane, R., Cardou, P., and Otis, M. J. D. Cable interference control in physical interaction for cable-driven parallel mechanisms, *Mechanism and Machine Theory*, **132**, 30–47, (2019). https://doi.org/10.1016/j.mechmachtheory.2018.10.002

[23] Ueland, E., Sauder, T., and Skjetne, R. Optimal force allocation for overconstrained cable-driven parallel robots: Continuously differentiable solutions with assessment of computational efficiency, *IEEE Transactions on Robotics*, **37** (2), 659–666, (2020). https://doi.org/10.1109/TRO.2020.3020747

[24] Shao, X. H. and Zhao, W. C. Relaxed modified Newton-based iteration method for generalized absolute value equations, *AIMS Mathematics*, **8** (2), 4714–4725, (2023). https://doi.org/10.3934/math.2023233

[25] Wu, L., Li, Z., Ge, W., and Zhao, X. An adaptive differential evolution algorithm with elite gaussian mutation and bare-bones strategy, *Mathematical Biosciences and Engineering*, **19** (8), 8537–8553, (2022). https://doi.org/10.3934/mbe.2022396

[26] Panagant, N., Pholdee, N., Bureerat, S., Yildiz, A. R., and Mirjalili, S. A comparative study of recent multi-objective metaheuristics for solving constrained truss optimisation problems, *Archives of Computational Methods in Engineering*, 1–17, (2021). https://doi.org/10.1007/s11831-021-09531-8

[27] Kaveh, A., Hamedani, K. B., and Hamedani, B. B. Optimal design of large-scale dome truss structures with multiple frequency constraints using success-history based adaptive differential evolution algorithm, *Periodica Polytechnica Civil Engineering*, **67** (1), 36–56, (2023). https://doi.org/10.3311/PPci.21147

[28] Nguyen-Van, S., Nguyen, K. T., Dang, K. D., Nguyen, N. T., Lee, S., and Lieu, Q. X. An evolutionary symbiotic organisms search for multiconstraint truss optimization under free vibration and transient behavior, *Advances in Engineering Software*, **160**, 103045, (2021). https://doi.org/10.1016/j.advengsoft.2021.103045

[29] Xue, H., Yu, H., Zhang, X., and Quan, Q. A novel method for structural lightweight design with topology optimization, *Energies*, **14** (14), 4367, (2021). https://doi.org/10.3390/en14144367

[30] Wang, Q., Han, H., Wang, C., and Liu, Z. Topological control for 2D minimum compliance topology optimization using SIMP method, *Structural and Multidisciplinary Optimization*, **65** (1), 38, (2022). https://doi.org/10.1007/s00158-021-03124-6

[31] da Silveira, O. A. A. and Palma, L. F. Some considerations on multi-material topology optimization using ordered SIMP, *Structural and Multidisciplinary Optimization*, **65** (9), 261, (2022). https://doi.org/10.1007/s00158-022-03379-7

[32] Xu, S., Liu, J., Zou, B., Li, Q., and Ma, Y. Stress constrained multi-material topology optimization with the ordered SIMP method, *Computer Methods in Applied Mechanics and Engineering*, **373**, 113453, (2021). https://doi.org/10.1016/j.cma.2020.113453

[33] Zuo, T., Han, H., and Liu, Z. Explicit tunnels and cavities control using SIMP and MMA in structural topology optimization, *Computer-Aided Design*, **158**, 103482, (2023). https://doi.org/10.1016/j.cad.2023.103482

[34] Hu, X., Li, Z., Bao, R., Chen, W., and Wang, H. An adaptive method of moving asymptotes for topology optimization based on the trust region, *Computer Methods in Applied Mechanics and Engineering*, **393**, 114202, (2022). https://doi.org/10.1016/j.cma.2021.114202

[35] Yan, K., Cheng, G. D., and Wang, B. P. Topology optimization of damping layers in shell structures subject to impact loads for minimum residual vibration, *Journal of Sound and Vibration*, **431**, 226–247, (2018). https://doi.org/10.1016/j.jsv.2018.06.003

[36] Yan, K. and Wang, B. P. Two new indices for structural optimization of free vibration suppression, *Structural and Multidisciplinary Optimization*, **61**, 2057–2075, (2020). https://doi.org/10.1007/s00158-019-02451-z